CrossMark

JM PAPERS

Role of the hierarchy of coherent structures in the transport of heavy small particles in turbulent channel flow

Yutaro Motoori[1],†, **ChiKuen Wong**[1] and **Susumu Goto**[1],†

[1]Graduate School of Engineering Science, Osaka University, 1-3 Machikaneyama, Toyonaka, Osaka 560-8531, Japan

To investigate the transport of heavy small particles (inertial particles) in high-Reynolds-number wall turbulence, we conduct direct numerical simulations of inertial particles in turbulent channel flow at the friction Reynolds number $Re_\tau = 1000$. In the statistically steady state, particles distribute inhomogeneously; particles with different relaxation times form voids with different sizes in the bulk of the flow, whereas they form streak-like clusters with different widths along the streamwise direction. To explore the origin of the multiscale voids and clusters of particles, we identify objectively the axes of tubular vortices and the spines of streaks with different sizes. These identifications enable us to show quantitatively that (i) vortices sweep out the particles of the relaxation time comparable with their turnover time, irrespective of their size and existing height, and that, among these particles, (ii) those swept out by wall-detached tubular vortices form clusters isotropically around them, whereas (iii) those swept out by wall-attached vortices are attracted by a nearby low-speed streak. These explain the reason why the multiscale clusterings are well described in terms of the local Stokes number defined by the turnover time of multiscale vortices. Furthermore, these descriptions of the particle transport give us a clear view to understand velocity statistics and wall-deposition mechanism of inertial particles in high-Reynolds-number wall turbulence.

Key words: multiphase and particle-laden flows, turbulent flows, turbulent boundary layers

1. Introduction

Heavy small particles, which are sometimes called inertial particles, distribute inhomogeneously in turbulent flow to form voids and clusters (Maxey 1987). When the velocity relaxation time of the particles is comparable with the Kolmogorov time scale of turbulence, they concentrate in the regions with low vorticity and high strain rate

† Email addresses for correspondence: y.motoori.es@osaka-u.ac.jp, s.goto.es@osaka-u.ac.jp

(Squires & Eaton 1990, 1991). This preferential concentration was observed in many experiments and numerical simulations; see the reviews by Balachandar & Eaton (2010), Monchaux, Bourgoin & Cartellier (2012), Gustavsson & Mehlig (2016) and references therein.

In high-Reynolds-number homogeneous turbulence, inertial particles with longer relaxation times form larger clusters (Yoshimoto & Goto 2007; Ireland, Bragg & Collins 2016; Petersen, Baker & Coletti 2019; Wang *et al.* 2020*b*). This observation suggests that the clustering mechanism can be described in terms of the centrifugal effects of coherent vortices with various sizes. Recently, Oka & Goto (2021) described multiscale clustering in terms of coarse-grained acceleration fields of turbulence by generalizing the sweep-stick mechanism (Goto & Vassilicos 2008). They also emphasized that the lifetime of vortices is another important parameter to describe particle clustering.

In contrast to studies of homogeneous turbulence, which is a model of turbulence away from solid walls, most of the studies on inertial particles in wall turbulence focus on the accumulation of particles to the wall. Even without gravity, particles tend to accumulate in the near-wall region. This is because particles in the regions with higher turbulent intensity move more quickly than those in the quiescent near-wall regions. We call this phenomenon turbophoresis (Caporaloni *et al.* 1975; Reeks 1983), which has been investigated numerically in many studies of particle dispersions in turbulent channel flow (e.g. Marchioli & Soldati 2002; Picciotto, Marchioli & Soldati 2005; Soldati & Marchioli 2009; Sardina *et al.* 2012*a*; Bernardini 2014; Sikovsky 2014; Johnson, Bassenne & Moin 2020), open channel flow (e.g. Narayanan *et al.* 2003), turbulent boundary layers (e.g. Sardina *et al.* 2012*b*) and turbulent pipe flow (e.g. Marchioli *et al.* 2003; Picano, Sardina & Casciola 2009). In particular, particles with velocity relaxation time comparable to the time scale of the buffer-layer coherent structures are affected by the turbophoresis. Soldati & Marchioli (2009) described the transport mechanism in terms of the coherent structures as follows. A sweep induced by quasi-streamwise vortices carries particles towards the wall. These particles are trapped in the viscous sublayer, or they are entrained again in the buffer layer by ejection. Since the ejection can carry many particles from the wall and it is accompanied by a low-speed streak, the particles form a cluster along the streak. In these transport processes, the particles trapped in the viscous sublayer deposit on the wall due to weak fluctuating velocity, which is called the diffusional deposition mechanism (Marchioli *et al.* 2003).

In contrast, since inertial particles with longer relaxation times are less likely to be trapped by quasi-streamwise vortices in the buffer layer, they can move near the wall faster than those affected by the turbophoresis. As a result, particles with long relaxation times keep the velocity comparable with the fluid velocity of the bulk, and they collide intensely with the wall or deposit on it. This wall-deposition mechanism is called the free-flight mechanism (Friedlander & Johnstone 1957; Brooke, Hanratty & McLaughlin 1994).

Studies on the inertial particles dispersed in low-Reynolds-number wall turbulence have revealed the wall-accumulation process and its relation to the buffer-layer coherent structures. However, there are only a few studies on inertial particles in turbulence at higher Reynolds numbers (e.g. $Re_\tau = u_\tau h/\nu \gtrsim 1000$, where u_τ is the skin-friction velocity, h is the channel half-width, and ν is the kinematic viscosity). For example, Bernardini (2014) conducted direct numerical simulations (DNS) of inertial particles in turbulent channel flow at $Re_\tau = 150$, 300, 550 and 1000. The analysis showed that even in high-Reynolds-number turbulence, buffer-layer structures contribute to the wall accumulation of particles with relaxation time comparable to the time scale of turbulence near the wall (i.e. the inner time scale). It is also known, on the other hand, that the

statistics of longer-relaxation-time particles are related to outer-layer flow structures. Sardina *et al.* (2012*b*) conducted DNS of particle dispersion in a turbulent boundary layer at $Re_\tau \approx 800$ to show the self-similarity of statistics of inertial particles. Wang & Richter (2019) conducted two-way coupled DNS of inertial particles in open channel flow at $Re_\tau = 550$ and 950. The authors showed that particles with high inertia enhance directly the very-large-scale motions (VLSM). In addition to these DNS studies, there is an experimental study by Berk & Coletti (2020) to examine the wall-normal profile of the concentration of small particles in a turbulent boundary layer at very high Reynolds numbers ($Re_\tau = 7000$–19 000). Their study suggested that large-scale motions might affect particle statistics in such high-Reynolds-number turbulence. Recent studies (e.g. Jie, Andersson & Zhao 2021; Scherer *et al.* 2022) have also observed the contribution to particle clustering from not only buffer-layer structures but also large-scale ones. However, we do not fully understand the transport mechanism of particles with different relaxation times in high-Reynolds-number wall turbulence.

Meanwhile, many DNS studies (e.g. del Álamo *et al.* 2006; Jiménez 2012, 2013, 2018; Lozano-Durán, Flores & Jiménez 2012; Schlatter *et al.* 2014) have revealed three-dimensional flow structures in single-phase wall turbulence. Our previous studies also revealed the generation mechanism of the hierarchy of coherent structures in a turbulent boundary layer at $Re_\tau \approx 1000$ (Motoori & Goto 2019, 2020) and turbulent channel flow at $Re_\tau = 4179$ (Motoori & Goto 2021). Wall-attached vortices, i.e. vortices with size comparable to their existing height, are composed of the hierarchy of quasi-streamwise (or hairpin) vortices. At each level of the hierarchy, these vortices are located beside the same-size low-speed streaks. We also showed that these wall-attached structures are generated by the hierarchical self-sustaining process. In addition, it is known that the hierarchy of wall-attached vortices is essential for the modelling of wall turbulence (see the review by Marusic & Monty 2019) and the description of self-similar turbulent statistics (Hwang 2015). On the other hand, wall-detached vortices are created through the energy cascading process. In particular, the generation mechanism of those in the log layer is similar to periodic turbulence without a wall (Goto, Saito & Kawahara 2017).

The key to revealing the generation mechanism of the multiscale nature of particle distributions is the extraction of the hierarchical flow structures in real space. In the present study, we examine the transport of inertial particles based on the hierarchy of coherent structures. The aims of this study are: (i) to reveal the concrete relation between the multiscale voids and clusters of particles and the hierarchy of coherent structures in the buffer and log layers in high-Reynolds-number wall turbulence; and (ii) to describe the physical mechanism of the transport of inertial particles. For these purposes, we conduct DNS of the dispersion of inertial particles in turbulent channel flow at $Re_\tau = 1000$.

In the rest of the present article, we first describe the numerical methods of DNS of turbulent channel flow (§ 2.1) and of particle tracking (§ 2.2). Next, we describe methods for identifying vortex axes and spines of the streaks in scale-decomposed turbulent fields (§ 3). Then we demonstrate spatial distributions of particles (§ 4.1), and we show quantitatively the relation between particles and multiscale wall-detached vortices (§ 4.2) and wall-attached vortices (§ 4.3). In addition, we show the contributions of multiscale low-speed streaks to forming multiscale clusters of particles (§ 4.4). We further investigate in § 5 the clustering process and statistics of particles in terms of the hierarchy of coherent structures.

Re_τ	(L_x, L_y, L_z)	(N_x, N_y, N_z)	$(\Delta x^+, \Delta y^+, \Delta z^+)$
1000	$(2\pi h, 2h, \pi h)$	(768, 768, 512)	(8.2, 0.52–5.0, 6.1)

Table 1. Numerical parameters of the DNS. Here, L_x, L_y and L_z are the sides of the computational domain, N_x, N_y and N_z are the numbers of grid points, and Δx^+, Δy^+ and Δz^+ are the resolutions.
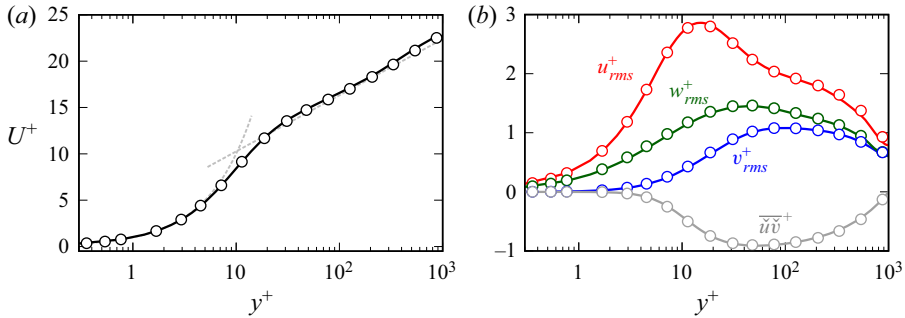

Figure 1. Wall-normal profiles of (*a*) the mean streamwise velocity and (*b*) the root-mean-square values of the fluctuating velocity components and the turbulent stress. Lines show the present results. Open circles show the results for the same Reynolds number in the Johns Hopkins Turbulence Databases (Graham *et al.* 2016). In (*a*), the grey dashed lines indicate the laws of the wall: $U^+ = y^+$ and $U^+ = (1/\kappa)\ln(y^+) + B$, with $\kappa = 0.368$ and $B = 3.67$.

2. Numerical simulation methods

2.1. *Direct numerical simulation of turbulent channel flow*

We simulate turbulent channel flow driven by a constant pressure gradient by solving the Navier–Stokes equations of an incompressible fluid. Since the target of the present study is a dilute dispersion of small particles, we neglect their effect on the fluid motion. The temporal integrations of the viscous and convection terms are made by using the second-order Crank–Nicolson method and the third-order Adams–Bashforth method, respectively. For spatial discretization of the terms in the governing equations, we use a sixth-order central difference scheme (Morinishi *et al.* 1998) on a staggered grid in the streamwise (x) and spanwise (z) directions, and a non-uniform finite difference scheme in the wall-normal (y) direction.

The numerical parameters of the DNS are listed in table 1. Here, a + superscript indicates the wall unit defined in terms of u_τ and ν. To investigate the dynamics of inertial particles affected by the hierarchy of vortices, we conduct DNS of the turbulence at sufficiently high Reynolds number $Re_\tau = 1000$. We show in figure 1 the wall-normal distributions of the mean streamwise velocity U (figure 1*a*) and the streamwise u_{rms}, wall-normal v_{rms} and spanwise w_{rms} root-mean-square values of the fluctuating velocity and the turbulent stress $\overline{\tilde{u}\tilde{v}}$ (figure 1*b*). These are in good agreement with the data in the Johns Hopkins Turbulence Databases (Graham *et al.* 2016).

2.2. *Particle tracking*

In the present study, we investigate the motion of rigid spherical particles in turbulence, which satisfy the following assumptions: (i) the mass density ρ_p of the particles is much larger than that ρ_f of fluid; (ii) the particle diameter d_p is smaller than the Kolmogorov

length scale η; and (iii) gravity is neglected. Under these assumptions, since we can neglect the effect of added mass, fluid acceleration and Basset history force on the motion of particles (Maxey & Riley 1983; Armenio & Fiorotto 2001), the equations of motion for the point particles are expressed as

$$\frac{\mathrm{d}\boldsymbol{x}_p}{\mathrm{d}t} = \boldsymbol{u}_p \tag{2.1a}$$

and

$$\frac{\mathrm{d}\boldsymbol{u}_p}{\mathrm{d}t} = -\frac{k_p}{\tau_p} (\boldsymbol{u}_p - \boldsymbol{u}). \tag{2.1b}$$

Here, $\boldsymbol{x}_p$ and $\boldsymbol{u}_p$ are the position and velocity of a particle, $\boldsymbol{u}$ is the fluid velocity at the particle position, and $\tau_p = \rho_p d_p^2/18\mu$ (where μ is the viscosity of the fluid) is the particle velocity relaxation time. Particles are subjected only to Stokes drag with nonlinear correction $k_p = 1 + 0.15 Re_p^{0.687}$ (Balachandar & Eaton 2010), where Re_p is the particle Reynolds number, i.e. $Re_p = d_p|\boldsymbol{u} - \boldsymbol{u}_p|/\nu$.

In the present study, we set the parameters to be the same as those used by Bernardini (2014). We assume that the working fluid is air with mass density $\rho_f = 1.3\,\mathrm{kg\,m^{-3}}$ and kinematic viscosity $\nu = 1.57 \times 10^{-5}\,\mathrm{m^2\,s^{-1}}$. We set the mass density of each particle as $\rho_p = 2700\rho_f$, which satisfies assumption (i). The particles are assumed to be heavy sand (e.g. olivine sand). Although the density may be larger than standard sand, for example, quartz sand with $\rho_p \approx 2200\rho_f$, we examine the case with $\rho_p = 2700\rho_f$, which is same as in Bernardini (2014). The most important parameter is the particle relaxation time τ_p, which is expressed in non-dimensional form as the Stokes number. We use the Stokes number $St_+ = \tau_p/\tau_+$ non-dimensionalized by the wall-unit time scale $\tau_+(= \nu/u_\tau^2)$ and examine seven cases with $St_+ = 1, 10, 25, 50, 100, 250$ and 1000. Since we fix the mass density ρ_p of particles, the diameter d_p is larger for larger Stokes numbers. Note, however, that even the diameter of the largest particle is of the order of the Kolmogorov scale (approximately the same as the wall-unit scale; see table 2), which satisfies assumption (ii). Costa, Brandt & Picano (2020) showed that the pointwise assumption affects the particle velocity statistics near the wall ($y/h \lesssim 0.1$ at $Re_\tau = 180$, i.e. $y^+ \lesssim 20$) but pointwise particles can capture the dynamics of the finite-size ($d_p^+ = 3$) particles in the bulk region ($y^+ \gtrsim 20$). Since the scope of the present study is to reveal the transport of particles in the buffer and log layers ($y^+ \gtrsim 30$), the pointwise assumption may be justified. The Froude number ($Fr_p = u_\tau/u_g$) defined by the ratio of the flow speed to the settling velocity u_g ($u_g = g\tau_p$, with g being the magnitude of gravitational acceleration) is larger than unity (see table 2). Although gravity affects the wall accumulation of particles even for $Fr_p \gg 1$ (Bragg, Richter & Wang 2021), since the objective of the present study is to reveal the origin of particle clusters and voids in the buffer and log layers, we assume the simple case that (iii) gravity is negligible. Numerical parameters are listed in table 2.

To track inertial particles, we integrate numerically (2.1) by using the second-order Adams–Bashforth method. The fluid velocity at the particle position is evaluated by linear interpolation. We inject $N = 10^7$ particles into turbulence in a statistically steady state. The initial particle positions are uniform. The initial velocity is set equal to the fluid velocity at the position of each particle. For the streamwise and spanwise directions, we impose periodic boundary conditions. When the distance of the particle centre from the wall becomes less than its radius, perfectly elastic collision is assumed to occur.

St_+	d_p^+	d_p (μm)	τ_p (s)	Fr_p
1	0.082	1.0	9.55×10^{-6}	1.37×10^4
10	0.25	3.2	9.55×10^{-5}	1.37×10^3
25	0.41	5.0	2.39×10^{-4}	5.47×10^2
50	0.58	7.1	4.78×10^{-4}	2.74×10^2
100	0.82	10.0	9.55×10^{-4}	1.37×10^2
250	1.83	22.4	4.78×10^{-3}	2.74×10
1000	2.58	31.6	9.55×10^{-3}	1.37×10

Table 2. Numerical parameters for the particles. The channel half-width is $h = 1.22$ cm.

Note that this assumption is violated in realistic situations (e.g. Joseph *et al.* 2001; Gondret, Lance & Petit 2002). The restitution coefficient between an elastic particle and a solid wall (e.g. a glass bead and an acrylic wall) depends on the Stokes number determined by the particle velocity at the collision. Due to the small restitution coefficient, all particles may deposit eventually on the wall, unless we reintroduce particles (Narayanan *et al.* 2003). In the present study, in order to simulate the statistically steady state for the particle distribution, we assume perfectly elastic collision, which was also used in many previous studies (e.g. Marchioli & Soldati 2002; Picano *et al.* 2009; Bernardini 2014). We will re-emphasize in § 5.2 that the restitution coefficient may affect the concentration profile.

As mentioned in the Introduction, particles tend to accumulate in the near-wall region due to the turbophoresis. To evaluate the inhomogeneity at time t, we calculate the Shannon entropy $S(t)$ (Picano *et al.* 2009). We divide the computational domain into $N_{layer} = 500$ layers in the wall-normal direction, and evaluate the local particle number N_i within each layer. The entropy of particle distribution is defined by

$$\mathcal{S} = - \sum_{i}^{N_{layer}} \frac{N_i}{N} \log \frac{N_i}{N}. \tag{2.2}$$

Note that when the distribution is homogeneous, $\mathcal{S}$ takes maximum $\mathcal{S}_{max} = \log N_{layer}$; and when all particles are in a single layer, $\mathcal{S} = 0$. We therefore define the normalized entropy by $S = \mathcal{S}/\mathcal{S}_{max}$, which varies between 0 (inhomogeneous state) and 1 (homogeneous state). Figure 2 shows $S(t)$ of particles with $St_+ = 1$, 10, 25, 50, 100, 250 and 1000. We see that $S(t)$ tends to be almost constant for $t^* \gtrsim 50$, where t^* denotes the outer time scale defined by u_τ and h. In the steady state, particles with $St_+ = 25$ distribute most inhomogeneously. This is consistent with the previous study by Bernardini (2014). For the analyses shown in § 4, we take the average in the statistically steady state ($t^* > 60$).

3. Identification of the hierarchy of coherent structures

Before showing the relation between the spatial distribution of particles and the hierarchy of coherent structures, we describe the methods of the objective identifications of the hierarchy of vortices and streaks in §§ 3.2 and 3.3, respectively. Since we use the filtered velocity in these methods, we first describe its numerical evaluation in § 3.1.
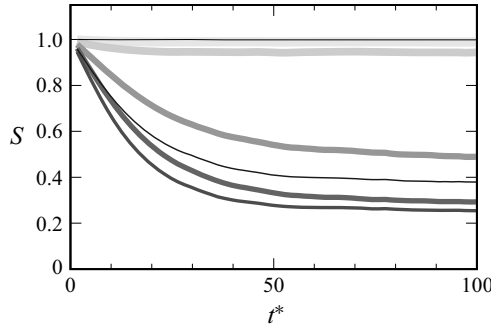
Figure 2. Time evolution of the normalized Shannon entropy. From thinner (and darker) to thicker (and lighter) lines, $St_+ = 1, 10, 25, 50, 100, 250$ and 1000.

3.1. *Scale decomposition*

To decompose the velocity field into different scales, we first apply a Gaussian filter

$$u_i^{(\sigma)low}(\boldsymbol{x}) = C_{filter}(\sigma) \int_V \check{u}_i(\boldsymbol{x}') \exp\left(-\frac{2}{\sigma^2}(\boldsymbol{x} - \boldsymbol{x}')^2\right) \mathrm{d}\boldsymbol{x}' \tag{3.1}$$

to the fluctuating velocity $\check{u}_i = u_i - U_i$, that is, the instantaneous velocity u_i minus the mean velocity U_i (averaged in the streamwise and spanwise directions and over time). Here, σ denotes the filter scale and $C_{filter}(\sigma)$ is the coefficient to ensure that the integration of the kernel is unity. For the wall-normal direction, we use the method proposed by Lozano-Durán, Holzner & Jiménez (2016) so that the filtering operation is extended by reflecting the filter at the walls, and the sign of $\check{u}_2(= \check{v})$ is inverted in order to satisfy the incompressibility and non-slip boundary condition of $v^{(\sigma)}$. Since $u_i^{(\sigma)low}$ captures the information of all the scales larger than σ, the filter corresponds to a low-pass filter of the Fourier modes of the velocity. We then take the difference between the low-pass filtered fields at two different scales, i.e.

$$u_i^{(\sigma)}(\boldsymbol{x}) = u_i^{(\sigma)low}(\boldsymbol{x}) - u_i^{(2\sigma)low}(\boldsymbol{x}). \tag{3.2}$$

This filter corresponds to a band-pass filter of the Fourier modes in the sense that $u_i^{(\sigma)}$ has the contributions from only around the scale σ. Note that we evaluate a scale-decomposed quantity $\cdot^{(\sigma)}$ (for example, the second invariant $Q^{(\sigma)}$ of the velocity gradient tensor) from $u_i^{(\sigma)}$. In our previous study (Motoori & Goto 2021), we demonstrated that the filtered velocity and its gradient captured the hierarchy of streaks and vortices, respectively.

3.2. *Vortex axes*

In the present study, by applying the low-pressure method (Miura & Kida 1997; Kida & Miura 1998a) to the filtered fields (3.2), we identify objectively the axes of tubular vortices with size σ. For this purpose, we solve the Poisson equation

$$\nabla^2 p^{(\sigma)} = -\nabla \cdot (\boldsymbol{u}^{(\sigma)} \cdot \nabla \boldsymbol{u}^{(\sigma)}), \tag{3.3}$$

whose source terms are expressed by $\boldsymbol{u}^{(\sigma)}$ to obtain the scale-decomposed pressure $p^{(\sigma)}$.

In the low-pressure method (Miura & Kida 1997; Kida & Miura 1998a), by connecting the points where the pressure takes the local minimum, we define the axis of the vortex. More precisely, the axis is composed of the points that attain the local minimum of the
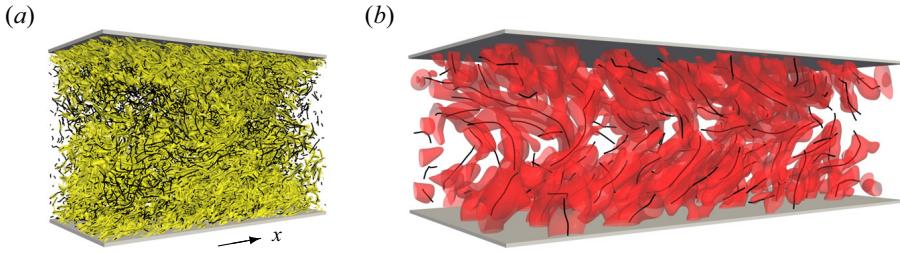
(*a*)   (*b*)

Figure 3. Axes of vortices at scales (*a*) $\sigma^+ = 30$ and (*b*) $\sigma^+ = 240$. Transparent yellow and red objects are isosurfaces of the second invariant $Q^{(\sigma)}/Q^{(\sigma)}_{rms} = 1$ of the velocity gradient tensor at the same scales. In (*a*), we visualize a subdomain (half in the streamwise and spanwise directions) of the computational domain.

pressure on the plane spanned by the first $e^{[1]}$ and second $e^{[2]}$ eigenvectors of the pressure Hessian. The other eigenvector $e^{[3]}$ is in the axial direction. Here, the superscript i of $e^{[i]}$ is assigned in ascending order of the eigenvalues $\lambda^{[i]}$ ($\lambda^{[1]} \geqslant \lambda^{[2]} \geqslant \lambda^{[3]}$). In the present study, we apply the method to the filtered fields of turbulent channel flow. The combination of a filter and the low-pressure method was also used by Goto *et al.* (2017) and Tsuruhashi *et al.* (2021) for periodic turbulence. Note that the Hessian is evaluated from the σ-scale pressure $p^{(\sigma)}$ in (3.3). We omit superscripts $\cdot^{(\sigma)}$ in the following.

From the centre x_0 in a grid cell, we find a candidate point $(x_0 + c)$ on the nearby vortex axis. Here, the vector c is taken to be perpendicular to the axis, i.e.

$$c \cdot e^{[3]} = 0. \tag{3.4}$$

Since the pressure at $x_0 + c$ takes the local minimum on the plane spanned by $e^{[1]}$ and $e^{[2]}$, c also satisfies

$$\nabla p(x_0 + c) \cdot e^{[\alpha]} = 0 \quad (\alpha = 1, 2). \tag{3.5}$$

By the Taylor expansion of the pressure gradient $\nabla p(x_0 + c)$, we rewrite (3.5) as

$$c \cdot e^{[\alpha]} = -e^{[\alpha]} \cdot \nabla p(x_0)/\lambda^{[\alpha]} \quad (\alpha = 1, 2). \tag{3.6}$$

By solving (3.4) and (3.6), we obtain a candidate point $(x_0 + c)$ for a vortex axis. We conduct the procedures for all the grid cells where $\lambda^{[2]} > 0$ (which is a necessary condition that the pressure takes a local minimum). When the identified point is located outside the grid cell containing x_0, we discard it. We also exclude points in irrotational regions (Kida & Miura 1998*b*).

To compose a vortex axis, we connect the points in the neighbouring grid cells if the angle between the segment and the rotational axis $e^{[3]}$ is smaller than $15°$, where the direction of $e^{[3]}$ is set so that $e^{[3]} \cdot \omega^{(\sigma)}$ is positive. We have confirmed that even if we set smaller angles such as $10°$, the identified vortex axes are almost identical to those in the present case. For the following analyses, we use only the composed vortex axes longer than σ.

We show in figure 3 the axes (black lines) of vortices with sizes $\sigma^+ = 30$ and 240. We see that the identified axes are located along the centre lines of yellow and red tubular objects, which are the positive isosurfaces of $Q^{(\sigma)}$. Thus the method can identify objectively the vortex axes without any threshold.

Incidentally, $\sigma^+ = 30$ is of the order of the smallest-scale vortices ($5\eta \lesssim \sigma \lesssim 20\eta$, with η being the Kolmogorov scale), whereas $\sigma^+ = 240$ is approximately the largest-scale vortices ($\sigma \approx h/4$). Our previous study (Motoori & Goto 2021) examined turbulent
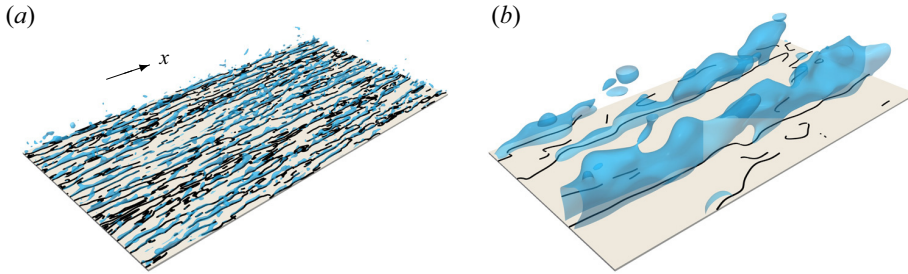
(*a*)

(*b*)

Figure 4. Spines of low-speed streaks at scales (*a*) $\sigma^+ = 30$ and (*b*) $\sigma^+ = 240$. Transparent blue objects are the negative isosurfaces of the streamwise fluctuating velocity (*a*) $u^{(\sigma)+} = -1.2$ and (*b*) $u^{(\sigma)+} = -0.6$ at the same scales. We visualize a subdomain (half in the wall-normal direction) of the computational domain.

channel flow at $Re_\tau = 4179$ obtained by DNS of Lozano-Durán & Jiménez (2014) to show that wall-attached ($\sigma \approx y$) vortices are quasi-streamwise vortices, whereas wall-detached ($\sigma < y$) vortices are distributed isotropically. These characteristics, which are indeed observed in figure 3, are important when we investigate particle clustering. In §§ 4.2 and 4.3, we use the identified axes to examine the spatial distribution of particles around vortices with four different sizes ($\sigma^+ = 30, 60, 120$ and 240).

3.3. *Streaks*

We investigate in § 4.4 the aggregation of particles into the hierarchy of low-speed streaks. For this purpose, we extract the spine (the centre line on the wall) of each streak. We identify lines composed of the local minima in the spanwise direction of $u^{(\sigma)}$ at the grid point closest to the wall, i.e. the points satisfying

$$\frac{\partial u^{(\sigma)}}{\partial z} = 0 \quad \text{and} \quad u^{(\sigma)} < 0. \tag{3.7a,b}$$

The black lines in figure 4 show the identified spines of streaks for the scales $\sigma^+ = 30$ and 240. We see that they are located under streaks at each scale. Similar methods were used by many authors (e.g. Schoppa & Hussain 2002; Lee *et al.* 2014; Lee, Sung & Zaki 2017; Kevin, Monty & Hutchins 2019).

4. Results

4.1. *Spatial distribution of particles*

We show in figure 5 the two-dimensional (y–z) spatial distributions of inertial particles with $St_+ = 10, 25, 100$ and 250 in the statistically steady state. We visualize only particles in a thin (200 wall units) layer. Particles with smaller St_+ values ($St_+ = 10$ and 25) form small voids and clusters, whereas for larger St_+ values ($St_+ = 100$ and 250), such smaller-size clustering is obscure. Instead, larger clusters are prominent for $St_+ = 100$ and 250. This multiscale nature is verified quantitatively in figure 6 by the average pair correlation function (e.g. Landau & Lifshitz 1980; Kostinski & Shaw 2001; Chen, Goto & Vassilicos 2006)

$$\mathcal{M} = \frac{\langle (\delta n)^2 \rangle_\ell}{\langle n \rangle_\ell^2} - \frac{1}{\langle n \rangle_\ell}, \tag{4.1}$$
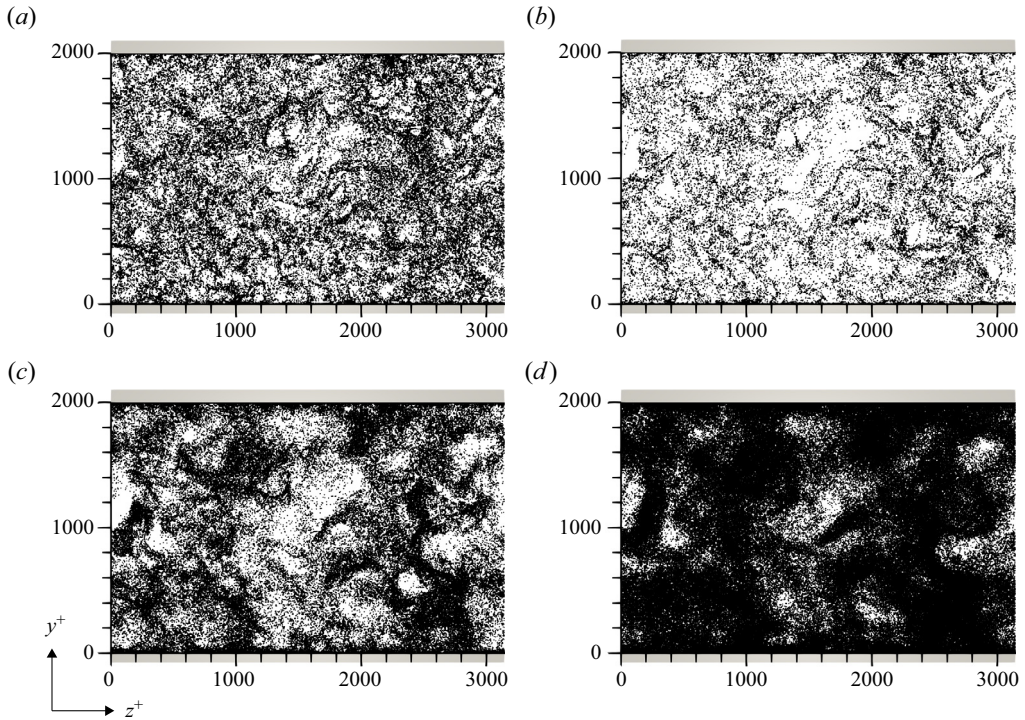
Figure 5. Two-dimensional (y–z) spatial distributions of particles with (a) $St_+ = 10$, (b) $St_+ = 25$, (c) $St_+ = 100$, and (d) $St_+ = 250$, within a streamwise layer of thickness 200 wall units.

where $\langle n \rangle_\ell$ and $\langle (\delta n)^2 \rangle_\ell (= \langle (n - \langle n \rangle_\ell)^2 \rangle_\ell)$ are, respectively, the average and variance of the number of particles in each box of size ℓ^3. If cluster size is sufficiently smaller than box size, then $\mathcal{M}$ becomes zero because n obeys the Poisson distribution with $\langle (\delta n)^2 \rangle_\ell = \langle n \rangle_\ell$. Therefore, $\mathcal{M}$ represents the size-ℓ-dependent clustering degree. We can see in both panels in figure 6 that around $\ell^+ \approx 10$, $\mathcal{M}$ values for $St_+ = 10$ and 25 (the second and third smallest circles) are larger than $St_+ = 100$ and 250. This means that particles with $St_+ = 10$ and 25 are more likely to form voids and clusters with size $\ell^+ \approx 10$ than $St_+ = 100$ and 250. In contrast, around $\ell^+ \approx 100$, $\mathcal{M}$ for $St_+ = 100$ (the fifth smallest circles in the insets of figure 6) is larger than $St_+ = 10$ and 25. These are consistent with the visualizations (figure 5). More precisely, comparing the results between figures 6(a) $200 \leq y^+ < 600$ and 6(b) $600 \leq y^+ < 1000$, farther away from the wall, particles with a given St_+ tend to create larger clusters. This multiscale clustering in the bulk region is similar to that in turbulence in a periodic cube (e.g. Yoshimoto & Goto 2007).

Comparing figures 5(b) $St_+ = 25$ and 5(d) 250, we notice that the numbers of particles in the bulk region are different. This is because particles with $St_+ = 25$ concentrate more near the walls through the turbophoresis. We show in figure 7 the average wall-normal concentration profile $c(y)$ in the statistically steady state, which is the ratio of the average number density of particles within a thin layer (4 wall units) to the bulk number density. Here, the average is taken over time and the homogeneous directions. We see that particles with $St_+ = 10$, 25 and 50 concentrate in the near-wall region. The observation is reasonable because these particles are carried by buffer-layer structures and trapped in the viscous sublayer ($y^+ \lesssim 5$) (Soldati & Marchioli 2009; Bernardini 2014).
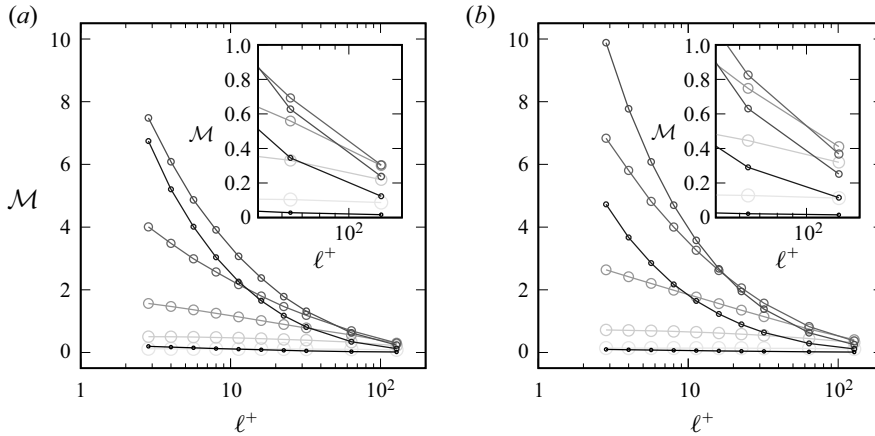
942 A3-10

Figure 6. Average pair correlation function of particles in the layers (*a*) $200 \leq y^+ < 600$ and (*b*) $600 \leq y^+ < 1000$. From smaller (and darker) to larger (and lighter) circles, $St_+ = 1$, 10, 25, 50, 100, 250 and 1000. The insets show the close-up for the range $\ell^+ \geq 50$.
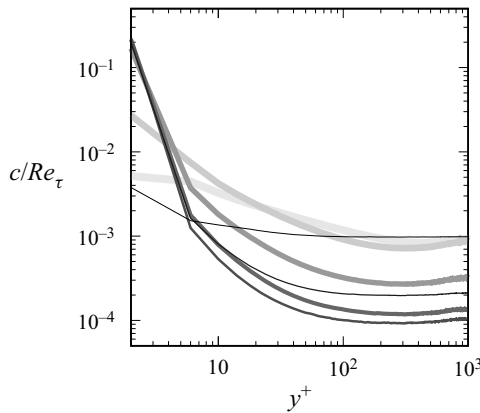

Figure 7. Average number density of particles as a function of height y^+. From thinner (and darker) to thicker (and lighter) lines, $St_+ = 1$, 10, 25, 50, 100, 250 and 1000.

Since the Reynolds number is high enough, in addition to buffer-layer vortices, wall-attached larger-size vortices and wall-detached vortices co-exist (see figure 3). In the following two subsections, to understand the role of the multiscale vortices in the transport of particles, we investigate the relationship between the observed multiscale clusterings and the hierarchy of vortices.

4.2. *Particle voids and the hierarchy of wall-detached vortices*

To show quantitatively the origin of multiscale clusterings of particles, we use the identification of vortex axes introduced in § 3.2. This enables us to evaluate the number of particles around the axis of each coherent vortex. In this subsection, we show the results for wall-detached vortices, i.e. vortices whose size σ is smaller than their existing height ($\sigma < y$). Since the vortex axes are distributed isotropically (Motoori & Goto 2021), we evaluate the number density $N_{p|vor}$ of particles as a function of the distance r from the vortex axes. For the conditional average, we set the bin width of r as $\Delta_{bin} = \sigma/6$.
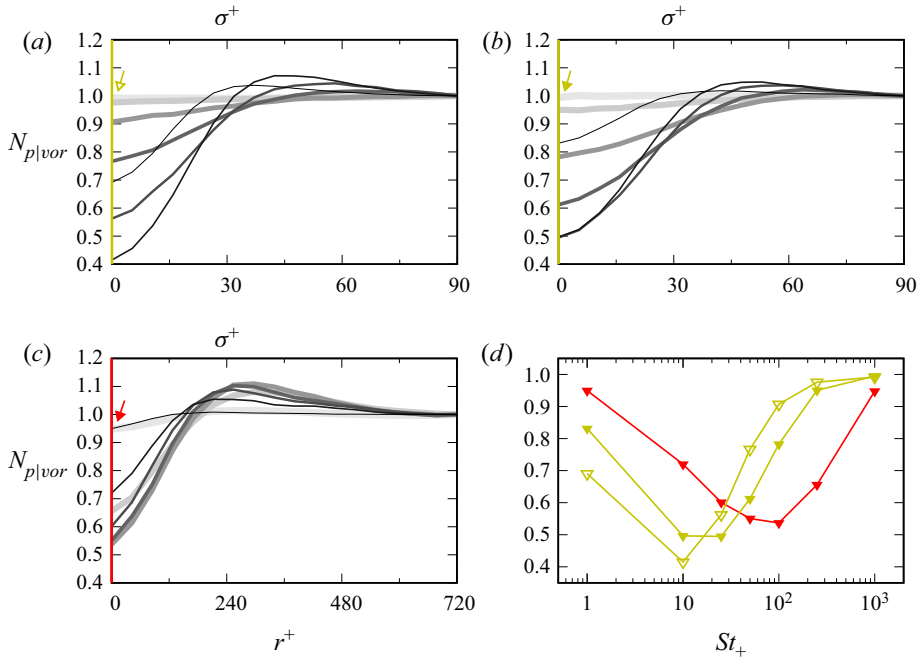
942 A3-11

Figure 8. Average number density of particles existing at distance r from an axis of vortices with sizes (a,b) $\sigma^+ = 30$ and (c) $\sigma^+ = 240$, in layers (a) $200 \leq y^+ < 400$ and (b,c) $800 \leq y^+ < 1000$. The values are normalized by that at $r = 3\sigma$. From thinner (and darker) to thicker (and lighter) lines, $St_+ = 1$, 10, 25, 50, 100, 250 and 1000. In (d), we show $N_{p|vor}(0)$, which is indicated by the arrows in the other panels: (a) yellow open triangles, (b) yellow closed triangles, and (c) red closed triangles, as functions of St_+.

We first show, in figure 8(a), $N_{p|vor}(r)$ around the axes of the small-size ($\sigma^+ = 30$; see figure 3a) vortices existing in the layer $200 \leq y^+ < 400$. The thinner (and darker) lines show the results for particles with smaller Stokes numbers. Since we have confirmed that $N_{p|vor}(r)$ is almost constant for $r \geq 3\sigma$ (i.e. particles are homogeneous for $r \geq 3\sigma$), we normalize the values by those at $r = 3\sigma$. Looking at the second thinnest line ($St_+ = 10$), we see that the number density takes the minimum at $r = 0$, whereas it takes the maximum around $\sigma \lesssim r \lesssim 2\sigma$. This tendency is also observed for particles with Stokes numbers (e.g. $St_+ = 1$ and 25) close to $St_+ = 10$. In contrast, the number density of particles with $St_+ \gtrsim 100$ is almost constant, irrespective of r. Hence in the layer $200 \leq y^+ < 400$, the small-size vortices are more likely to sweep out particles with $St_+ \approx 10$.

Next, looking at the results for vortices with $\sigma^+ = 30$ for the higher height $800 \leq y^+ < 1000$ (figure 8b), we can see that the vortices sweep out predominantly particles of $St_+ = 25$. We replot in figure 8(d) the values at $r = 0$ with yellow triangles, which are indicated by the arrows in figures 8(a,b), as functions of St_+. It is clear that vortices with the same size but at different heights do not necessarily contribute to creating voids of particles with the same relaxation time.

Figure 8(c) shows $N_{p|vor}$ around vortices with a large size ($\sigma^+ = 240$) within the layer $800 \leq y^+ < 1000(= h^+)$. The results are for particles around the heads ($y \approx h$) of quasi-streamwise vortices (see figure 3b), and we call them wall-detached vortices in the sense that $\sigma < y$. We see in figure 8(c) that particles with $St_+ = 100$ are swept out most significantly, and they form clusters around the vortices ($r \approx \sigma$). Red triangles in

942 A3-12

figure 8(*d*) show $N_{p|vor}(0)$ as a function of St_+ indicated by the arrow in figure 8(*c*). Comparing the three lines, vortices with different sizes and heights create voids of particles with different St_+.

In addition to figure 8(*d*), we plot in figure 9(*a*) $N_{p|vor}(0)$ for vortices at the fixed size $\sigma^+ = 30$ in four different layers. We also show in figure 9(*b*) the results for the vortices with four different sizes ($\sigma^+ = 30, 60, 120$ and 240) in the fixed layer $800 \leq y^+ < 1000$. These two panels show that for larger sizes or farther distance from the wall (shown by the lighter lines), the vortices tend to sweep out particles with larger St_+. Note that the well of each line shifts to larger St_+. This implies that vortices sweep out particles of the relaxation time comparable with their turnover time. To verify this quantitatively, we define the time scale $\tau_Q = 1/\sqrt{Q_{rms}^{(\sigma)}}$ of vortices in terms of the root-mean-square value $Q_{rms}^{(\sigma)}(y)$ of the second invariant of the velocity gradient tensor at scale σ. Note that the time scale is a function of y and σ. We then define the local Stokes number by

$$St_Q(\sigma, y) = \frac{\tau_p}{\tau_Q(\sigma, y)}. \tag{4.2}$$

The quantities shown in figures 9(*c*) and 9(*d*) are the same as in figures 9(*a,b*) but as functions of St_Q instead of St_+. Here, we have used the value of τ_Q at the centre in each layer. We see that the minimum of the curve collapses around $St_Q \approx 0.2$. We can therefore conclude that, irrespective of the existing height and size, vortices preferentially sweep out particles of the relaxation time τ_p comparable with the turnover time τ_Q. This observation around wall-detached vortices is similar to that in homogeneous turbulence (Bec *et al.* 2007; Yoshimoto & Goto 2007; Wang *et al.* 2020*b*; Oka & Goto 2021). The importance of the time scale matching was also pointed out by Soldati & Marchioli (2009) for the clustering in the buffer layer in low-Reynolds-number turbulence.

The Kolmogorov second similarity hypothesis gives the time scale τ_v of vortices with size σ in the inertial range as

$$\tau_v^+(\sigma, y) \sim (\sigma^+)^{2/3} (\epsilon^+)^{-(1/3)}. \tag{4.3}$$

Here, ϵ is the mean energy dissipation rate. For turbulent channel flow, if we assume equilibrium between the energy dissipation ϵ and the energy production, the log law of the mean velocity profile and $-\overline{\tilde{u}\tilde{v}}^+ \approx 1$ in the log layer (Rotta 1962), then the energy dissipation rate is estimated by

$$\epsilon^+ \sim -\overline{\tilde{u}\tilde{v}}^+ \frac{\partial U^+}{\partial y^+} \approx (\kappa y^+)^{-1}. \tag{4.4}$$

Therefore, we can rewrite (4.3) as

$$\tau_v^+(\sigma, y) \sim (\sigma^+)^{2/3} (y^+)^{1/3}. \tag{4.5}$$

We have evaluated in figures 9(*c,d*) the turnover time of the vortices with size σ and at height y in terms of τ_Q. We show in figure 10(*a*) that τ_Q obeys the scaling (4.5) in the inertial range in the log layer. The thinner (and darker) grey lines indicate the time scale of smaller-size vortices, and the blue dashed lines with the same thickness indicate τ_v (see (4.5)) for the same σ. Looking at the thinnest grey and blue lines ($\sigma^+ = 30$), we see that they are overlapped for $60 \lesssim y^+ \lesssim 200$. For $y^+ \gtrsim 200$, where the lines do not overlap, the scale $\sigma^+ = 30$ is in the dissipation range ($\sigma \lesssim 10\eta$). The two lines for $\sigma^+ = 60$ are also in
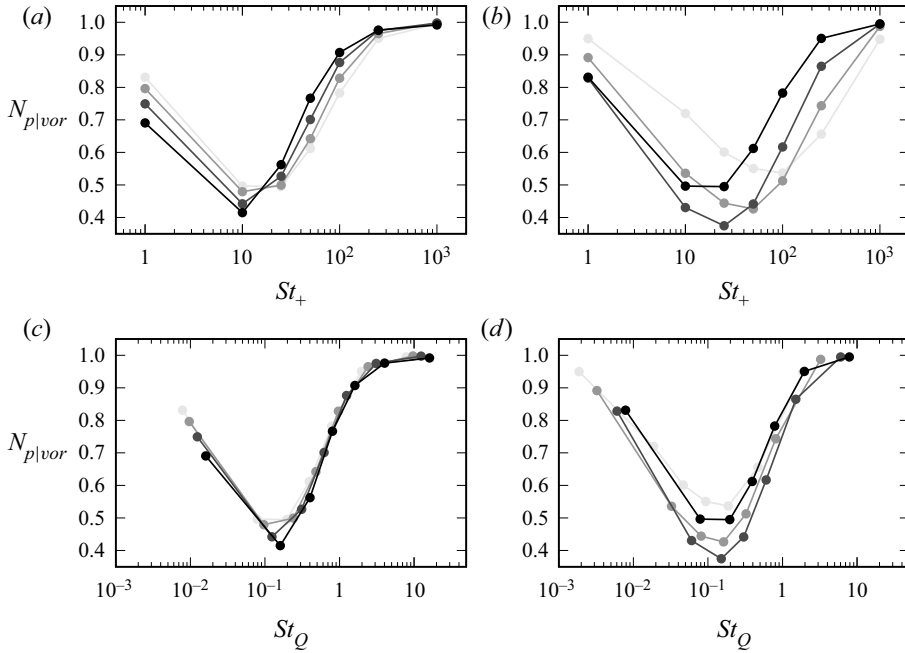
Figure 9. Average number density of particles existing in the region ($0 \leq r < \Delta_{bin}$, where $\Delta_{bin} = \sigma/6$) near an axis of (*a,c*) vortices with fixed size $\sigma^+ = 30$ in the different layers $200 \leq y^+ < 400$ (black), $400 \leq y^+ < 600$ (dark grey), $600 \leq y^+ < 800$ (light grey) and $800 \leq y^+ < 1000$ (very light grey), and (*b,d*) vortices with the different sizes $\sigma^+ = 30$ (black grey), $\sigma^+ = 60$ (dark grey), $\sigma^+ = 120$ (light grey) and $\sigma^+ = 240$ (very light grey) in the fixed layer $800 \leq y^+ < 1000$. The values are functions of (*a,b*) St_+, and (*c,d*) St_Q.
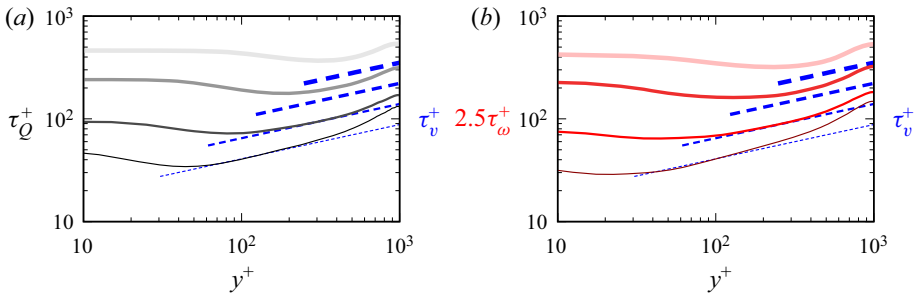

Figure 10. Time scales evaluated by (*a*) τ_Q and (*b*) τ_ω of vortices with size σ and height y. Note that in (*b*), we plot $2.5\tau_\omega^+$ to fit the blue dashed lines: $\tau_v^+ = C(\sigma^+)^{2/3}(y^+)^{1/3}$ with $C = 0.9$. From thinner (and darker) to thicker (and lighter) lines, $\sigma^+ = 30$, 60, 120 and 240.

good agreement for $120 \lesssim y^+ \lesssim 400$. Therefore, in the inertial range in the log layer (e.g. $10\eta \lesssim \sigma \lesssim y/2$), τ_Q obeys the scaling (4.5). Incidentally, the time scale $\tau_\omega = 1/\sqrt{\omega_i^{(\sigma)2}}$ is similar to τ_Q (figure 10*b*), which might be easier to estimate.

We summarize the results in this subsection. In turbulent channel flow, wall-detached vortices ($\sigma < y$) most effectively sweep out particles of the relaxation time comparable with their turnover time irrespective of their size (figure 9*d*) and their existing height (figure 9*c*). Hence the origin of the multiscale voids is the hierarchy of vortices, and we can explain the multiscale nature in terms of time scale matching between particles
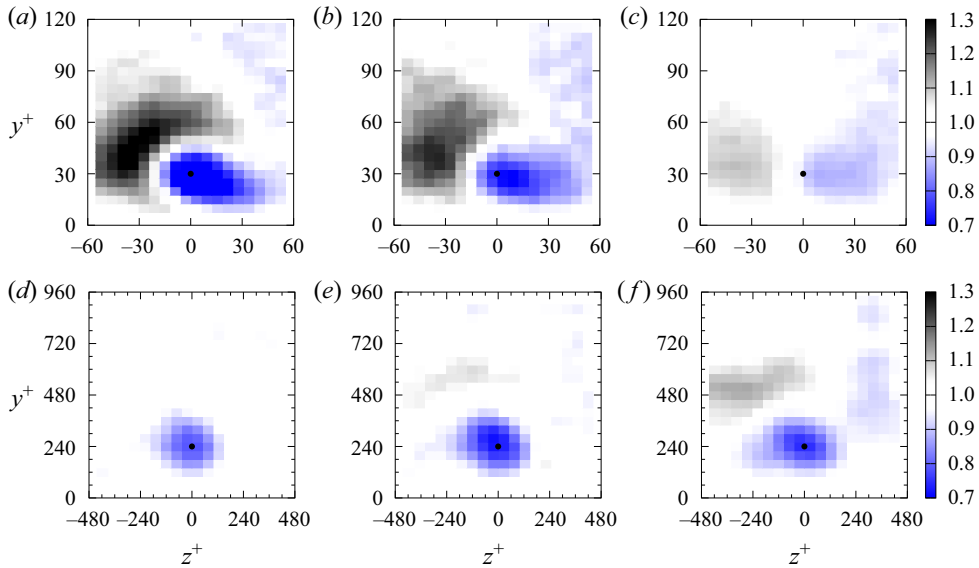
942 A3-14

Figure 11. Average number density of particles with (a,d) $St_+ = 10$, (b,e) $St_+ = 25$, and (c,f) $St_+ = 100$, in the y–z plane around an axis (black closed circle) of quasi-streamwise vortices with sizes $(a$–$c)$ $\sigma^+ = 30$ and $(d$–$f)$ $\sigma^+ = 240$, with positive streamwise vorticity (clockwise rotation). The values are non-dimensionalized by the average number density at each height.

and vortices. We may use the scale-decomposed velocity gradients (e.g. enstrophy and the second invariant of the velocity gradient tensor) to estimate the turnover times of vortices (figure 10). In the next subsection, to show the importance of the time scale matching for wall-attached vortices ($\sigma = y$), we examine particle clustering around quasi-streamwise vortices with various sizes.

4.3. *Particle voids and the hierarchy of wall-attached vortices*

In order to investigate multiscale voids and clusters created by the hierarchy of wall-attached quasi-streamwise vortices, we show the two-dimensional (y–z) distribution of particles around quasi-streamwise vortices. First, we show results for quasi-streamwise vortices with positive streamwise vorticity in the buffer layer. Figures 11(a–c) show the conditionally averaged number density – more precisely, the number density of particles around the axes of vortices rotating clockwise at $\sigma^+ = 30$ and $y^+ = 30$. The values are normalized by the average number density at each height. We see in figure 11(a) that the number of particles with $St_+ = 10$ is smaller around the vortex core (black closed circle). In contrast, the particles form a cluster in the left region in the panel, where strong ejection is induced by the vortices. This means that in the buffer layer ($y^+ \approx 30$), quasi-streamwise vortices (with size $\sigma^+ \approx 30$) sweep out particles with $St_+ = 10$ from their cores, and the nearby ejection carries particles away from the wall. As a result, the particles form clusters in low-speed streaks. In other words, the creation mechanism of particle voids is the same as that by wall-detached vortices (§ 4.2), whereas the formed clusters are inhomogeneous in the spanwise direction due to a nearby low-speed streak. This result implies that the clustering mechanism in terms of coherent structures described by Soldati & Marchioli (2009) holds in the buffer layer irrespective of the Reynolds number. The
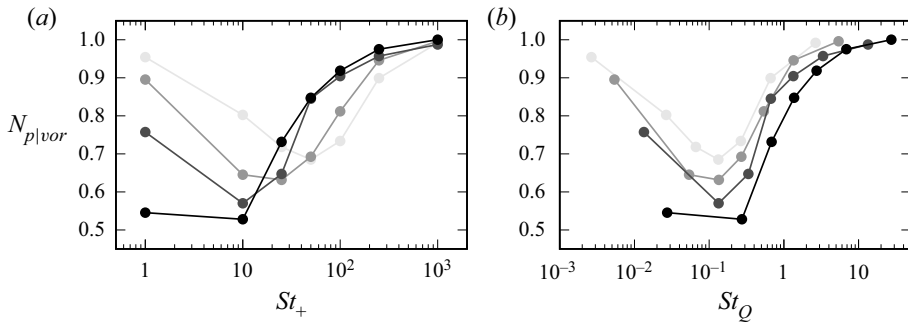
Figure 12. Average number density of particles existing in the region ($y = \sigma$ and $z = 0$) on an axis of quasi-streamwise vortices with sizes $\sigma^+ = 30$ (black), $\sigma^+ = 60$ (dark grey), $\sigma^+ = 120$ (light grey) and $\sigma^+ = 240$ (very light grey) at height $y = \sigma$ as functions of (*a*) St_+ and (*b*) St_Q.

clustering degree becomes weaker for particles with longer relaxation times $St_+ = 25$ (figure 11*b*) and $St_+ = 100$ (figure 11*c*).

Next, figures 11(*d–f*) show results for quasi-streamwise vortices with a larger size $\sigma^+ = 240$. In contrast to the results for buffer-layer-size vortices, the channel-half-width-size vortices more predominantly sweep out the particles with $St_+ = 100$ (figure 11*f*) than $St_+ = 10$ (figure 11*d*). We also show in figure 12 the number density on the axis (black closed circle) for $\sigma^+ = 30$, 60, 120 and 240 as functions of St_+ and St_Q. We observe that the values take the minimum around $St_Q \approx 0.2$ irrespective of the size of vortices. This observation is the same as that for wall-detached vortices (figure 9). We therefore conclude that, irrespective of the size, existing height and type (wall-detached or wall-attached) vortices, the time scale matching is the key to the creation of multiscale voids in high-Reynolds-number wall turbulence.

We emphasize that the results for wall-attached vortices are consistent with the previous study (Bernardini 2014) on the wall-deposition process of particles in turbulent channel flow. Particles with $St_+ \approx 10$ are swept out from quasi-streamwise vortices in the buffer layer (figure 11*a*), whereas larger-size vortices hardly sweep out these particles (figure 11*c*). This implies that even if the Reynolds number increases – that is, the number of the levels in the hierarchy of wall-attached vortices increases – such larger-size vortices do not contribute to the transport of particles with $St_+ \approx 10$ from and to the wall. This is the reason why the wall-deposition process (i.e. the so-called diffusional deposition mechanism) of particles with $St_+ \approx 10$ is universal irrespective of the Reynolds number, as was shown by Bernardini (2014). In contrast, large-size quasi-streamwise vortices can transport particles with larger St_+ ($\gtrsim 100$, figure 11*f*). This is also consistent with the fact shown by Bernardini (2014) that the wall-deposition rates of particles with $St_+ \gtrsim 100$ are determined by the Stokes number $St_o = \tau_p u_\tau / h$ defined by the turbulent time scale in the outer layer (i.e. the so-called free-flight mechanism).

As was mentioned above, clusters formed by wall-attached vortices tend to be formed in the ejections. This means that particles swept out by quasi-streamwise vortices are likely to be accumulated in low-speed streaks. We indeed observe the multiscale attraction into the streaks in figure 13, which shows the two-dimensional (*x–z*) spatial distributions of particles with $St_+ = 10$ and 250. Particles for larger St_+ form larger-size streamwise-elongated clusters. In the next subsection, we investigate further the multiscale attraction mechanism of particles by low-speed streaks with different sizes.
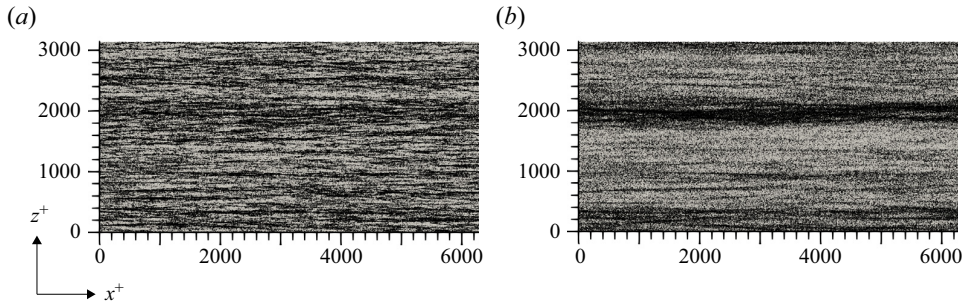
942 A3-16

Figure 13. Two-dimensional (x–z) spatial distributions of particles with (a) $St_+ = 10$ and (b) $St_+ = 250$, within $0 < y^+ < 50$.
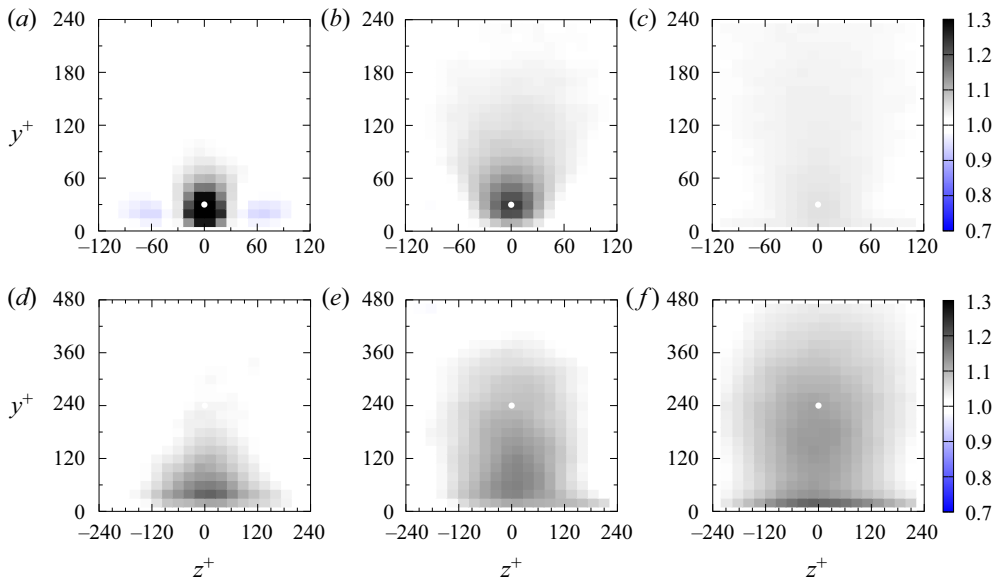

Figure 14. Average number density of particles with (a,d) $St_+ = 10$, (b,e) $St_+ = 100$ and (c,f) $St_+ = 1000$, in the y–z plane around a spine of the low-speed streak at the sizes (a–c) $\sigma^+ = 30$ and (d–f) $\sigma^+ = 240$. The values are non-dimensionalized by the average number density at each height.

4.4. *Particle clusters and the hierarchy of streaks*

To verify quantitatively that multiscale low-speed streaks contribute to the attraction of particles, we show the average number density $N_{p|low}$ in the y–z plane around spines of low-speed streaks. The identification method has been introduced in § 3.3.

We show, in figures 14(a–c), $N_{p|low}$ around low-speed streaks at scale $\sigma^+ = 30$. The number density is normalized by the average at each height. The number of particles with $St_+ = 10$ (figure 14a) is larger in the region around the white closed circle ($y = \sigma$ and $z = 0$). This implies that the particles are likely to concentrate in low-speed streaks. It is also important that the trend is weaker for particles with longer relaxation times $St_+ = 100$ (figure 14b) and $St_+ = 1000$ (figure 14c). In contrast, we see in figures 14(d–f) that low-speed streaks with a larger size ($\sigma^+ = 240$) attract particles with longer relaxation times $St_+ = 100$ (figure 14e) and $St_+ = 1000$ (figure 14f).
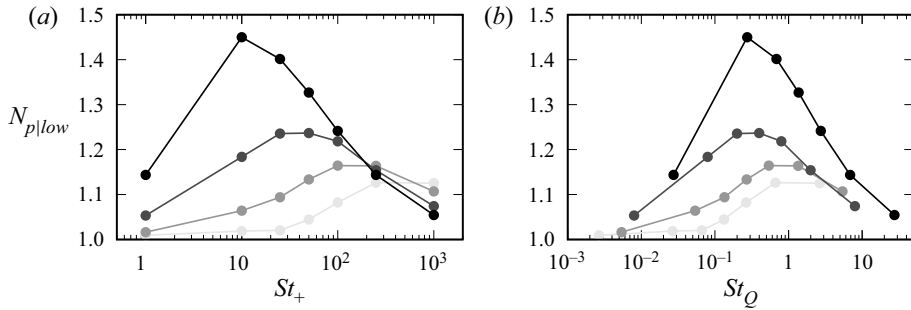
Figure 15. Average number density of particles existing in the region ($y = \sigma$ and $z = 0$) on a spine of low-speed streaks with sizes $\sigma^+ = 30$ (black), $\sigma^+ = 60$ (dark grey), $\sigma^+ = 120$ (light grey) and $\sigma^+ = 240$ (very light grey), at the height $y = \sigma$ as functions of (*a*) St_+ and (*b*) St_Q.

Moreover, we show in figure 15(*a*) the values at the centre (white closed circle) of the low-speed streaks as functions of St_+. Lighter lines show the results for larger sizes ($\sigma^+ = 30$, 60, 120 and 240). As expected from figure 14, larger-size streaks contribute to the attraction of particles of larger St_+ into their centre. Figure 15(*b*) shows the same quantities as in figure 15(*a*) but as functions of the local Stokes number St_Q (see (4.2)). The number of the particles takes the maximum in a range $0.2 \lesssim St_Q \lesssim 2$ irrespective of the size of streaks. Therefore, we conclude that the hierarchy of low-speed streaks attracts particles of the relaxation time comparable with the turnover time of accompanying quasi-streamwise vortices. In other words, at each level of the hierarchy, particles are swept out from quasi-streamwise vortices (§ 4.3), and they form clusters in a nearby low-speed streak.

Before closing this subsection, it is worth mentioning that the clusters formed by smaller-size streaks are much more prominent (figure 14), although this is not clear in the visualizations (figure 13). This observation is consistent with the result that smaller-size quasi-streamwise vortices tend to form stronger clusters (figure 12). This is because smaller-size wall-attached vortices (i.e. those in the buffer layer) are more likely to carry particles from the viscous sublayer, where particles concentrate most (see figure 7), to the bulk.

5. Discussions

5.1. *Description of multiscale clustering in terms of multiscale vortices*

We have shown that the time scale matching between particles and vortices is most important to explain multiscale clustering. In this subsection, we demonstrate that a simple argument based on the equations of motion leads to the same conclusion. For this purpose, we introduce imaginary particles (Oka & Goto 2021) that obey

$$\frac{\mathrm{d}\boldsymbol{x}_p^*}{\mathrm{d}t} = \boldsymbol{u}_p^* \tag{5.1a}$$

and

$$\frac{\mathrm{d}\boldsymbol{u}_p^*}{\mathrm{d}t} = -\frac{1}{\tau_p}(\boldsymbol{u}_p^* - \boldsymbol{u}^{(\sigma)low}). \tag{5.1b}$$

Here, $\boldsymbol{x}_p^*$ and $\boldsymbol{u}_p^*$ are the position and velocity of the imaginary particles, respectively, and $\boldsymbol{u}^{(\sigma)low}$ is the velocity field coarse-grained at the scale σ (see (3.1)). The imaginary particles

942 A3-18

are affected only by velocity larger than σ. This model is consistent with the present results (e.g. figures 5 and 8) that larger-scale clusters are formed around larger-scale vortices. Therefore, it is reasonable to assume that the clusters of real particles governed by (2.1) are similar to those of imaginary particles governed by (5.1). Incidentally, by simulating the imaginary particles in periodic turbulence, our previous studies (Oka & Goto 2021; Oka, Watanabe & Goto 2021) verified this assumption numerically. Here, we extend this argument to wall turbulence.

First, by applying the argument of Maxey (1987) to (5.1), we express the relative velocity of particles to fluid as

$$\boldsymbol{u}_p^* - \boldsymbol{u}^{(\sigma)low} \approx -\tau_p \boldsymbol{a}^{(\sigma)low}. \tag{5.2}$$

Here, $\boldsymbol{a}^{(\sigma)low}$ is the coarse-grained acceleration of fluid. Note that (5.2) yields under the condition that τ_p is sufficiently smaller than $T(\sigma; y)$, where $T(\sigma; y)$ is the eddy turnover time for size σ and height y. As shown in figure 10, since we estimate T by τ_Q, (5.2) holds for $\tau_p \lesssim \tau_Q(\sigma; y)$. Then, taking the divergence of (5.2), we obtain

$$-\nabla \cdot \boldsymbol{u}_p^* \approx \tau_p (\nabla \cdot \boldsymbol{a}^{(\sigma)low}). \tag{5.3}$$

The left-hand side implies the accumulation rate $\gamma(= -\nabla \cdot \boldsymbol{u}_p^*)$ of the particles when considering them as a continuum. In other words, the particles accumulate in the region satisfying $\gamma > 0$, whereas the particles are swept out from the region satisfying $\gamma < 0$. In the inertial range, since the acceleration is approximated by the pressure gradient (i.e. $\boldsymbol{a}^{(\sigma)low} \approx -(1/\rho_f) \nabla p^{(\sigma)low}$), we can rewrite (5.3) as

$$-\nabla \cdot \boldsymbol{u}_p^* \approx -\tau_p \left(\frac{1}{\rho_f} \nabla^2 p^{(\sigma)low} \right) = -\tau_p Q^{(\sigma)low}. \tag{5.4}$$

Hence the accumulation rate is determined by $Q^{(\sigma)low}$, that is, particles are swept out from rotational regions ($Q^{(\sigma)low} > 0$), whereas they accumulate in irrotational regions ($Q^{(\sigma)low} < 0$). Moreover, if we estimate $Q^{(\sigma)low}$ by τ_Q^{-2}, then we can evaluate the order of the clustering time $T_{cluster}(= 1/\gamma)$ as

$$T_{cluster} \approx \frac{\tau_Q^2(\sigma, y)}{\tau_p}. \tag{5.5}$$

It takes $T_{cluster}$ for particles with τ_p to be swept out from vortices with the turnover time $\tau_Q(\sigma, y)$. If $T_{cluster}$ is shorter than the lifetime T_{life} of vortices, then the particles are swept out completely. Therefore, a necessary condition for forming voids and clusters is given by

$$T_{cluster} \lesssim T_{life} \quad \Longleftrightarrow \quad \frac{\tau_Q^2(\sigma, y)}{T_{life}(\sigma, y)} \lesssim \tau_p. \tag{5.6}$$

Next, recall that (5.2) holds under the condition $\tau_p \lesssim \tau_Q(\sigma, y)$. We then obtain the clustering condition

$$\frac{\tau_Q^2(\sigma, y)}{T_{life}(\sigma, y)} \lesssim \tau_p \lesssim \tau_Q(\sigma, y). \tag{5.7}$$

Vortices with eddy turnover time τ_Q and lifetime T_{life} sweep out effectively particles with relaxation time τ_p satisfying condition (5.7). If we assume that T_{life} is proportional to τ_Q, then we conclude that vortices are most likely to sweep out particles with $\tau_p \approx \tau_Q$.

This is the reason why the local Stokes number $St_Q(= \tau_p/\tau_Q)$ is important for the clustering condition. Recall that in the inertial range of the log layer, the scaling $\tau_Q \sim \sigma^{2/3}y^{1/3}$ holds (see § 4.2). Therefore, we can predict that particles with a given relaxation time τ_p at height y are swept out from vortices with size $\sigma \sim \tau_p^{3/2}y^{-(1/2)}$. We emphasize that the scaling is also valid for much higher Reynolds number wall-turbulence because there is a wide range of the log layer. Incidentally, under the assumption $T_{life} \approx \tau_Q$, since the clustering time (see (5.5)) is estimated as $T_{cluster} \approx \tau_Q(\approx \tau_p)$, larger vortices take longer time to form particle clusters. This is consistent with the results by Liu *et al.* (2020) that the lifetime of the clusters is also longer for larger ones.

Furthermore, it is worth mentioning that since it takes a finite time to sweep out particles, the created voids can be located in different regions from present vortices. This history effect is important especially in streamwise inhomogeneous turbulence (e.g. adverse-pressure-gradient turbulent boundary layers).

5.2. *Particle velocity statistics*

The above results and discussions suggest that the hierarchy of coherent structures plays an important role in transporting inertial particles. By using this, in the present subsection, we explain the particle velocity statistics, which determine the wall-normal distribution of particles (such as shown in figure 7), in terms of the scale-dependent fluid velocity.

As described in detail by Johnson *et al.* (2020), if we assume that the particle Reynolds number is sufficiently small (i.e. when the Stokes drag coefficient k_p in (2.1*b*) is unity), then the wall-normal concentration $c(y)$ of particles in the statistically steady state is written as

$$c(y) = \frac{\mathcal{N}}{\langle v_p^2 \mid y \rangle} \exp \left(\frac{1}{\tau_p} \int^y \frac{\langle v \mid \xi \rangle}{\langle v_p^2 \mid \xi \rangle} \, \mathrm{d}\xi \right). \tag{5.8}$$

Here, $\mathcal{N}$ is an integration constant, and $\langle \cdot \mid y \rangle$ denotes the average sampled by the position of particles $y = y_p$; namely, $\langle v_p^2 \mid y \rangle$ is the variance of the wall-normal particle velocity, and $\langle v \mid y \rangle$ is the mean wall-normal fluid velocity at $y = y_p$. If the relaxation time of particles is sufficiently large ($\tau_p^{-1} \to 0$), we can approximate (5.8) as

$$c(y) \approx \frac{\mathcal{N}}{\langle v_p^2 \mid y \rangle}. \tag{5.9}$$

This implies that $\langle v_p^2|y \rangle$ determines the concentration of particles for larger St_+. Johnson *et al.* (2020) showed that (5.9) is a good approximation for $St_+ \gtrsim 128$ in low-Reynolds-number turbulent channel flow ($Re_\tau = 150$).

As has been discussed in the previous subsection (§ 5.1), we consider the imaginary particles that obey (5.1). Since the relative velocity of particles to fluid is expressed by (5.2) under the condition $\tau_p \ll T(\sigma; y)$, we can approximate $\langle v_p^2 \mid y \rangle$ as

$$\langle v_p^2 \mid y \rangle \approx \langle (v^{(\sigma)low} - \tau_p a_y^{(\sigma)low})^2 \mid y \rangle \approx \langle v^{(\sigma)low2} \mid y \rangle. \tag{5.10}$$

In addition to this approximation in the zeroth order of τ_p, if we assume homogeneity (i.e. $\langle v^{(\sigma)low2} \rangle \approx \langle v^{(\sigma)low2} \mid y \rangle$), then we can estimate $\langle v_p^2 \mid y \rangle$ in terms of the scale-dependent fluid information of $\langle v^{(\sigma)low2} \rangle$. Here, we choose the filter scale σ so that it satisfies
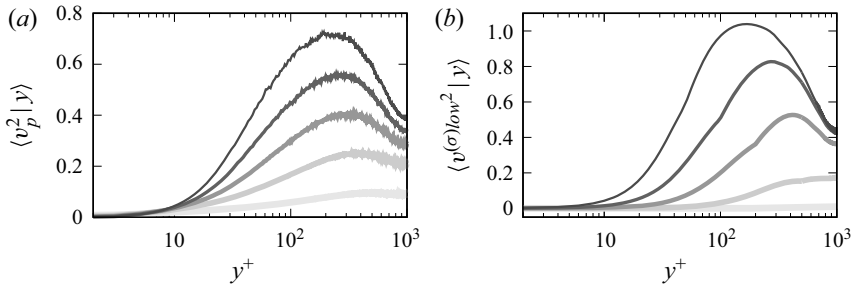
942 A3-20

Figure 16. (*a*) Variance of the wall-normal particle fluctuating velocity. (*b*) Variance of the wall-normal fluid velocity at scales $\sigma(\tau_p; y)$ satisfying $T = \tau_p$, where T is expressed by (5.11). From thinner (and darker) to thicker lines, $St_+ = 25, 50, 100, 250$ and 1000.

$T(\sigma; y) = \tau_p$, where T is expressed by

$$T = C\sigma^{2/3}y^{1/3} \quad \text{if } y \geq 2\sigma, \tag{5.11a}$$

$$T = 2^{1/3}C\sigma \qquad \text{if } y < 2\sigma, \tag{5.11b}$$

with $C = 0.9$. This expression is based on the results shown in figure 10.

We show in figures 16(*a,b*) the left- and right-hand sides of (5.10), respectively; that is, figure 16(*a*) shows the variance $\langle v_p^2 \,|\, y \rangle$ of the wall-normal velocity of particles with $St_+ = 25, 50, 100, 250$ and 1000, and figure 16(*b*) shows the variance $\langle v^{(\sigma)low2} \rangle$ of wall-normal fluid velocity coarse-grained at different scales $\sigma(\tau_p; y)$ satisfying $T(\sigma; y) = \tau_p$. It is clear that these two quantities for $St_+ = 25$–100 behave in a similar manner, which implies that (5.10) gives a good approximation. We therefore conclude that we can describe the variance $\langle v_p^2 \,|\, y \rangle$ of particle velocity in terms of $\langle v^{(\sigma)low2} \rangle$ by choosing σ that satisfies $T(\sigma; y) = \tau_p$. More concretely, for $y \gtrsim 2\sigma$, the ratio between these quantities is almost constant. This means that (5.11*a*) is a good expression for the time scale of wall-detached vortices. In contrast, for $y \lesssim 2\sigma$, $\langle v_p^2 \,|\, y \rangle$ is larger than $\langle v^{(\sigma)low2} \rangle$. This is because the transport of particles for $y \ll \sigma$ is determined by other factors, for example, the foot ($y \ll \sigma$) of wall-attached vortices. However, it is hard to quantify their effects from the scale-decomposed turbulent fields obtained by the present coarse-graining method. Note that we do not show $\langle v^{(\sigma)low2} \rangle$ for $St_+ = 1$ and 10 in figure 16, since the corresponding filter scale σ is smaller than the grid width.

Incidentally, to predict the wall-normal concentration $c(y)$ (see (5.8)) of particles by using $\langle v^{(\sigma)low2} \rangle$, we need to take into account the effect of the viscous sublayer, where particles concentrate most (see figure 7). Moreover, when the Stokes number is small, the approximation (5.9) is invalid, and $\langle v \,|\, y \rangle$ is another factor determining the concentration (see (5.8)). These detailed studies are left for a future study. Furthermore, although we have employed the assumption of perfectly elastic collisions between particles and solid walls, in a more realistic situation, this assumption is invalid (Joseph *et al.* 2001; Gondret *et al.* 2002). The difference in the restitution coefficient may affect the concentration profile.

6. Conclusions

To investigate the transport mechanism of inertial particles in high-Reynolds-number turbulent channel flow, we have conducted DNS of those with seven relaxation times ($St_+ = 1, 10, 25, 50, 100, 250$ and 1000) in turbulence at $Re_\tau = 1000$. The key ingredient

of our analysis is the objective identification of the hierarchy of coherent flow structures (§ 3). By using this, we have shown the average distribution of particles around the axes of vortices (§§ 4.2 and 4.3) and around the spines of streaks (§ 4.4) at each level of the hierarchy. The analyses lead to revealing the role of coherent structures in the multiscale clusterings of particles. Vortices create particle voids with the size of themselves by sweeping out particles of the relaxation time comparable with their turnover time. This mechanism holds irrespective of the size, existing height and type (wall-detached or wall-attached) of vortices. Hence the multiscale clusterings are determined by the local Stokes numbers ($St_Q \approx 0.2$) at any level of the hierarchy of vortices (figures 9c,d). We have also shown that particles swept out by wall-detached tubular vortices form clusters isotropically around them, whereas those swept out by wall-attached vortices are attracted by a nearby low-speed streak (figures 12b and 15b). Particles swept out by smaller-size wall-attached vortices form denser clusters (figures 11, 12 and 15) because smaller-size (buffer-layer-size) vortices carry particles from the wall. In § 5.1, extending the arguments (Oka & Goto 2021; Oka *et al.* 2021) of particle clustering in periodic turbulence to wall turbulence, we have also demonstrated that the above clustering mechanism is explained in terms of the imaginary particles advected by the filtered velocity. We have also explained the velocity statistics and concentration profile of inertial particles in terms of the hierarchy of coherent flow structures (§ 5.2).

Declaration of interests. The authors report no conflict of interest.

Author ORCIDs.
ⓘ Yutaro Motoori https://orcid.org/0000-0002-9647-9014;
ⓘ Susumu Goto https://orcid.org/0000-0001-7013-7967.

REFERENCES

DEL ÁLAMO, J.C., JIMÉNEZ, J., ZANDONADE, P. & MOSER, R.D. 2006 Self-similar vortex clusters in the turbulent logarithmic region. *J. Fluid Mech.* **561**, 329–358.

ARMENIO, V. & FIOROTTO, V. 2001 The importance of the forces acting on particles in turbulent flows. *Phys. Fluids* **13**, 2437–2440.

BALACHANDAR, S. & EATON, J.K. 2010 Turbulent dispersed multiphase flow. *Annu. Rev. Fluid Mech.* **42**, 111–133.

BEC, J., BIFERALE, L., CENCINI, M., LANOTTE, A., MUSACCHIO, S. & TOSCHI, F. 2007 Heavy particle concentration in turbulence at dissipative and inertial scales. *Phys. Rev. Lett.* **98**, 084502.

BERK, T. & COLETTI, F. 2020 Transport of inertial particles in high-Reynolds-number turbulent boundary layers. *J. Fluid Mech.* **903**, A18.

BERNARDINI, M. 2014 Reynolds number scaling of inertial particle statistics in turbulent channel flows. *J. Fluid Mech.* **758**, R1.

BRAGG, A., RICHTER, D. & WANG, G. 2021 Settling strongly modifies particle concentrations in wall-bounded turbulent flows even when the settling parameter is asymptotically small. *Phys. Rev. Fluids* **6**, 124301.

BROOKE, J.W., HANRATTY, T.J. & McLAUGHLIN, J.B. 1994 Free-flight mixing and deposition of aerosols. *Phys. Fluids* **6**, 3404–3415.

CAPORALONI, M., TAMPIERI, F., TROMBETTI, F. & VITTORI, O. 1975 Transfer of particles in nonisotropic air turbulence. *J. Atmos. Sci.* **32**, 565–568.

CHEN, L., GOTO, S. & VASSILICOS, J.C. 2006 Turbulent clustering of stagnation points and inertial particles. *J. Fluid Mech.* **553**, 143–154.

COSTA, P., BRANDT, L. & PICANO, F. 2020 Interface-resolved simulations of small inertial particles in turbulent channel flow. *J. Fluid Mech.* **883**, A54.

FRIEDLANDER, S.K. & JOHNSTONE, H.F. 1957 Deposition of suspended particles from turbulent gas streams. *Ind. Engng Chem.* **49**, 1151–1156.

GONDRET, P., LANCE, M. & PETIT, L. 2002 Bouncing motion of spherical particles in fluids. *Phys. Fluids* **14**, 643–652.

GOTO, S., SAITO, Y. & KAWAHARA, G. 2017 Hierarchy of antiparallel vortex tubes in spatially periodic turbulence at high Reynolds numbers. *Phys. Rev. Fluids* **2**, 064603.

GOTO, S. & VASSILICOS, J.C. 2008 Sweep-stick mechanism of heavy particle clustering in fluid turbulence. *Phys. Rev. Lett.* **100**, 054503.

GRAHAM, J., *et al.* 2016 A web services-accessible database of turbulent channel flow and its use for testing a new integral wall model for LES. *J. Turbul.* **17**, 181–215.

GUSTAVSSON, K. & MEHLIG, B. 2016 Statistical models for spatial patterns of heavy particles in turbulence. *Adv. Phys.* **65**, 1–57.

HWANG, Y. 2015 Statistical structure of self-sustaining attached eddies in turbulent channel flow. *J. Fluid Mech.* **767**, 254–289.

IRELAND, P.J., BRAGG, A.D. & COLLINS, L.R. 2016 The effect of Reynolds number on inertial particle dynamics in isotropic turbulence. Part 1. Simulations without gravitational effects. *J. Fluid Mech.* **796**, 617–658.

JIE, Y., ANDERSSON, H.I. & ZHAO, L. 2021 Effects of the quiescent core in turbulent channel flow on transport and clustering of inertial particles. *Intl J. Multiphase Flow* **140**, 103627.

JIMÉNEZ, J. 2012 Cascades in wall-bounded turbulence. *Annu. Rev. Fluid Mech.* **44**, 27–45.

JIMÉNEZ, J. 2013 Near-wall turbulence. *Phys. Fluids* **25**, 101302.

JIMÉNEZ, J. 2018 Coherent structures in wall-bounded turbulence. *J. Fluid Mech.* **842**, P1.

JOHNSON, P.L., BASSENNE, M. & MOIN, P. 2020 Turbophoresis of small inertial particles: theoretical considerations and application to wall-modelled large-eddy simulations. *J. Fluid Mech.* **883**, A27.

JOSEPH, G.G., ZENIT, R., HUNT, M.L. & ROSENWINKEL, A.M. 2001 Particle–wall collisions in a viscous fluid. *J. Fluid Mech.* **433**, 329–346.

KEVIN, K., MONTY, J. & HUTCHINS, N. 2019 The meandering behaviour of large-scale structures in turbulent boundary layers. *J. Fluid Mech.* **865**, R1.

KIDA, S. & MIURA, H. 1998a Identification and analysis of vortical structures. *Eur. J. Mech. B/Fluids* **17**, 471–488.

KIDA, S. & MIURA, H. 1998b Swirl condition in low-pressure vortices. *J. Phys. Soc. Japan* **67**, 2166–2169.

KIM, J., MOIN, P. & MOSER, R. 1987 Turbulence statistics in fully developed channel flow at low Reynolds number. *J. Fluid Mech.* **177**, 133–166.

KOSTINSKI, A.B. & SHAW, R.A. 2001 Scale-dependent droplet clustering in turbulent clouds. *J. Fluid Mech.* **434**, 389–398.

LANDAU, L. & LIFSHITZ, E. 1980 *Statistical Physics*. Pergamon.

LEE, J., LEE, J.H., CHOI, J.I. & SUNG, H.J. 2014 Spatial organization of large- and very-large-scale motions in a turbulent channel flow. *J. Fluid Mech.* **749**, 818–840.

LEE, J., SUNG, H.J. & ZAKI, T.A. 2017 Signature of large-scale motions on turbulent/non-turbulent interface in boundary layers. *J. Fluid Mech.* **819**, 165–187.

LIU, Y., SHEN, L., ZAMANSKY, R. & COLETTI, F. 2020 Life and death of inertial particle clusters in turbulence. *J. Fluid Mech.* **902**, R1.

LOZANO-DURÁN, A., FLORES, O. & JIMÉNEZ, J. 2012 The three-dimensional structure of momentum transfer in turbulent channels. *J. Fluid Mech.* **694**, 100–130.

LOZANO-DURÁN, A., HOLZNER, M. & JIMÉNEZ, J. 2016 Multiscale analysis of the topological invariants in the logarithmic region of turbulent channels at a friction Reynolds number of 932. *J. Fluid Mech.* **803**, 356–394.

LOZANO-DURÁN, A. & JIMÉNEZ, J. 2014 Effect of the computational domain on direct simulations of turbulent channels up to $Re_\tau = 4200$. *Phys. Fluids* **26**, 011702.

MARCHIOLI, C., GIUSTI, A., SALVETTI, M.V. & SOLDATI, A. 2003 Direct numerical simulation of particle wall transfer and deposition in upward turbulent pipe flow. *Intl J. Multiphase Flow* **29**, 1017–1038.

MARCHIOLI, C. & SOLDATI, A. 2002 Mechanisms for particle transfer and segregation in a turbulent boundary layer. *J. Fluid Mech.* **468**, 283–315.

MARUSIC, I. & MONTY, J.P. 2019 Attached eddy model of wall turbulence. *Annu. Rev. Fluid Mech.* **51**, 49–74.

MAXEY, M.R. 1987 The gravitational settling of aerosol particles in homogeneous turbulence and random flow fields. *J. Fluid Mech.* **174**, 441–465.

MAXEY, M.R. & RILEY, J.J. 1983 Equation of motion for a small rigid sphere in a nonuniform flow. *Phys. Fluids* **26**, 883–889.

MIURA, H. & KIDA, S. 1997 Identification of tubular vortices in turbulence. *J. Phys. Soc. Japan* **66**, 1331–1334.

MONCHAUX, R., BOURGOIN, M. & CARTELLIER, A. 2012 Analyzing preferential concentration and clustering of inertial particles in turbulence. *Intl J. Multiphase Flow* **40**, 1–18.

MORINISHI, Y., LUND, T.S., VASILYEV, O.V. & MOIN, P. 1998 Fully conservative higher order finite difference schemes for incompressible flow. *J. Comput. Phys.* **143**, 90–124.

MOTOORI, Y. & GOTO, S. 2019 Generation mechanism of a hierarchy of vortices in a turbulent boundary layer. *J. Fluid Mech.* **865**, 1085–1109.

MOTOORI, Y. & GOTO, S. 2020 Hairpin vortices in the largest scale of turbulent boundary layers. *Intl J. Heat Fluid Flow* **86**, 108658.

MOTOORI, Y. & GOTO, S. 2021 Hierarchy of coherent structures and real-space energy transfer in turbulent channel flow. *J. Fluid Mech.* **911**, A27.

NARAYANAN, C., LAKEHAL, D., BOTTO, L. & SOLDATI, A. 2003 Mechanisms of particle deposition in a fully developed turbulent open channel flow. *Phys. Fluids* **15**, 763–775.

OKA, S. & GOTO, S. 2021 Generalized sweep-stick mechanism of inertial-particle clustering in turbulence. *Phys. Rev. Fluids* **6**, 044605.

OKA, S., WATANABE, D. & GOTO, S. 2021 Large-scale clustering of light small particles in developed turbulence. *Phys. Fluids* **33**, 031707.

PETERSEN, A.J., BAKER, L. & COLETTI, F. 2019 Experimental study of inertial particles clustering and settling in homogeneous turbulence. *J. Fluid Mech.* **864**, 925–970.

PICANO, F., SARDINA, G. & CASCIOLA, C.M. 2009 Spatial development of particle-laden turbulent pipe flow. *Phys. Fluids* **21**, 093305.

PICCIOTTO, M., MARCHIOLI, C. & SOLDATI, A. 2005 Characterization of near-wall accumulation regions for inertial particles in turbulent boundary layers. *Phys. Fluids* **17**, 098101.

REEKS, M.W. 1983 The transport of discrete particles in inhomogeneous turbulence. *J. Aero. Sci.* **14**, 729–739.

ROTTA, J.C. 1962 Turbulent boundary layers in incompressible flow. *Prog. Aerosp. Sci.* **2**, 1–95.

SARDINA, G., SCHLATTER, P., BRANDT, L., PICANO, F. & CASCIOLA, C.M. 2012a Wall accumulation and spatial localization in particle-laden wall flows. *J. Fluid Mech.* **699**, 50–78.

SARDINA, G., SCHLATTER, P., PICANO, F., CASCIOLA, C.M., BRANDT, L. & HENNINGSON, D.S. 2012b Self-similar transport of inertial particles in a turbulent boundary layer. *J. Fluid Mech.* **706**, 584–596.

SCHERER, M., UHLMANN, M., KIDANEMARIAM, A.G. & KRAYER, M. 2022 On the role of turbulent large-scale streaks in generating sediment ridges. *J. Fluid Mech.* **930**, A11.

SCHLATTER, P., LI, Q., ÖRLÜ, R., HUSSAIN, F. & HENNINGSON, D.S. 2014 On the near-wall vortical structures at moderate Reynolds numbers. *Eur. J. Mech. B/Fluids* **48**, 75–93.

SCHOPPA, W. & HUSSAIN, F. 2002 Coherent structure generation in near-wall turbulence. *J. Fluid Mech.* **453**, 57–108.

SIKOVSKY, D.P. 2014 Singularity of inertial particle concentration in the viscous sublayer of wall-bounded turbulent flows. *Flow Turbul. Combust.* **92**, 41–64.

SOLDATI, A. & MARCHIOLI, C. 2009 Physics and modelling of turbulent particle deposition and entrainment: review of a systematic study. *Intl J. Multiphase Flow* **35**, 827–839.

SQUIRES, K.D. & EATON, J.K. 1990 Particle response and turbulence modification in isotropic turbulence. *Phys. Fluids A* **2**, 1191–1203.

SQUIRES, K.D. & EATON, J.K. 1991 Preferential concentration of particles by turbulence. *Phys. Fluids A* **3**, 1169–1178.

TSURUHASHI, T., GOTO, S., OKA, S. & YONEDA, T. 2021 Self-similar hierarchy of coherent tubular vortices in turbulence. *Phil. Trans. R. Soc. A* **380**, 20210053.

WANG, G., PARK, H.J. & RICHTER, D.H. 2020a Effect of computational domain size on inertial particle one-point statistics in open channel flow. *Intl J. Multiphase Flow* **125**, 103195.

WANG, G. & RICHTER, D.H. 2019 Two mechanisms of modulation of very-large-scale motions by inertial particles in open channel flow. *J. Fluid Mech.* **868**, 538–559.

WANG, X., WAN, M., YANG, Y., WANG, L.-P. & CHEN, S. 2020b Reynolds number dependence of heavy particles clustering in homogeneous isotropic turbulence. *Phys. Rev. Fluids* **5**, 124603.

YOSHIMOTO, H. & GOTO, S. 2007 Self-similar clustering of inertial particles in homogeneous turbulence. *J. Fluid Mech.* **577**, 275–286.